

Constraining the systematics of (acoustic) wave heating estimates in the solar chromosphere

MOMCHIL E. MOLNAR,^{1,2,3,*} KEVIN P. REARDON,^{1,2} STEVEN R. CRANMER,^{2,3} ADAM F. KOWALSKI,^{1,2,3} AND IVAN MILIĆ^{4,1}

¹*National Solar Observatory, Boulder, Colorado, USA*

²*Department of Astrophysical and Planetary Sciences, University of Colorado, Boulder, USA*

³*Laboratory for Atmospheric and Space Physics, University of Colorado, Boulder, USA*

⁴*Astronomical Observatory, Belgrade, Serbia*

(Received February 9, 2023; Revised XXX; Accepted XXX)

Submitted to ApJ

ABSTRACT

Acoustic wave heating is believed to contribute significantly to the missing energy input required to maintain the solar chromosphere in its observed state. We studied the propagation of waves above the acoustic cutoff in the upper photosphere into the chromosphere with ultraviolet and optical spectral observations interpreted through comparison with three dimensional radiative magnetohydrodynamic (rMHD) *Bifrost* models to constrain the heating contribution from acoustic waves in the solar atmosphere. Sit-and-stare observations taken with the Interface Region Imaging Spectrograph (IRIS) and data from the Interferometric BIdimensional Spectrograph (IBIS) were used to provide the observational basis of this work. We compared the observations with synthetic observables derived from the Bifrost solar atmospheric model. Our analysis of the *Bifrost* simulations show that internetwork and enhanced network regions exhibit significantly different wave propagation properties, which are important for the accurate wave flux estimates. The inferred wave energy fluxes based on our observations are not sufficient to maintain the solar chromosphere. We point out that the systematics of the modeling approaches in the literature lead to differences which could determine the conclusions of this type of studies, based on the same observations.

1. INTRODUCTION

The solar chromosphere has a higher temperature than expected from radiative equilibrium (Withbroe & Noyes 1977; Carlsson et al. 2019). The additional heating required to maintain the chromosphere in its observed thermodynamic state is approximately a few to tens of kW/m², depending on the activity of the particular solar feature (Athay 1976; Díaz Baso et al. 2021). Understanding the primary heating sources is important for modeling the solar chromosphere correctly, as these will determine its structure and observed properties. This is an important astrophysical question beyond the Sun, because stellar chromospheres are the source of the UV continuum that influences their surrounding environment, e.g. dictates the atmospheric chemical composition of their exoplanets (Linsky 2017).

Previous work has suggested that the two most viable mechanisms to provide the missing heating in the solar atmosphere is through stochastic release of stored magnetic energy or dissipation of magnetohydrodynamic (MHD) waves. Release of magnetic energy – either through current sheet dissipation (Socas-Navarro 2005; Louis et al. 2021) or magnetic reconnection (Innes et al. 1997; Rouppe van der Voort et al. 2017) has been reported throughout the chromosphere with limited global heating implications. Conclusive observational evidence of this heating process is still lacking, even if models predict it to be pervasive in the active Sun (da Silva Santos et al. 2022).

In this paper we focus on the other possible heating mechanism – acoustic wave energy dissipation. Chromospheric heating by waves was proposed in the late 1940's (Biermann 1946; Schatzman 1949) and has been discussed extensively in the literature (see Aschwanden 2019, for a short review). Recent progress on constraining the wave heating in the solar chromosphere has been enabled by the technological advances of adaptive op-

Corresponding author: Momchil Molnar
mmolnar@ucar.edu

* Currently at the High Altitude Observatory, NCAR.

tics, tunable filtergraphs and more sensitive ultraviolet (UV) and near-infrared (IR) instruments. There are two differing conclusions about the energetic significance of acoustic waves in the lower solar atmosphere. In general, the body of work based on high-cadence Doppler velocity observations interpreted with a 1D static atmospheric perturbative approach derive wave fluxes sufficient to maintain the quiet chromosphere (e.g. Bello González et al. 2009; Sobotka et al. 2016; Abbasvand et al. 2020b). On the other hand, studies based on Doppler velocities from and UV/mm continuum observations interpreted with 1D time-dependent radiative hydrodynamic (rHD) models, well suited for chromospheric studies, come to the opposite conclusion – acoustic waves do not carry sufficient energy flux to maintain the quiet chromosphere (Fossum & Carlsson 2005; Carlsson et al. 2007; Molnar et al. 2021). However, the latter studies have been critiqued for systematic biases toward underestimating the acoustic flux (Wedemeyer-Böhm et al. 2007).

For this project, we extended the previous work on determining the acoustic wave flux in the chromosphere with optical observations of Molnar et al. (2021) (henceforth Paper I) with UV data of the low and high chromosphere from the Interface Region Imaging Spectrograph (IRIS, De Pontieu et al. 2014). We also used 3D instead of 1D radiative MHD (rMHD) models to interpret the wave observations. This could be considered an extension of the similar work by Abbasvand et al. (2021) with the inclusions of multiple spectral lines in the IRIS UV spectral sampling interval, instead of relying on the wings of the Mg II h and k lines. We argue that the interpretation of the observed oscillatory signals requires the use of 3D MHD models, contrary to 1D models used in previous work. Wave modeling that relies on 1D semi-empirical models (such as those of Fontenla et al. 2011) calculate the properties of the observed waves as perturbations on a static atmosphere, which may be an inaccurate approximation, if the dynamical oscillations are maintaining the atmosphere in a dynamic state far from equilibrium (see Bertschinger & Chevalier 1985, for a treatment of the similar physical setting on Mira-like stars).

This paper describes the observed wave properties in the lower and upper chromosphere observed in the UV with IRIS and tries to infer the energy flux of acoustic waves propagating in these regions through comparison with spectral synthesis from 3D rMHD Bifrost models (Gudiksen et al. 2011). We compared those results with diagnostics from the optical part of the spectrum obtained with the Imaging BiDimensional Spectrograph (IBIS, Cavallini 2006). The paper is organized in the

following way: Section 2 describes the UV and optical observations used throughout the paper; Section 3 presents the derived properties of the power spectra of different diagnostics; Section 4 presents the wave diagnostics derived from synthetic observables from *Bifrost* MHD enhanced network models; Section 5 discusses the systematics between different modeling approaches. We conclude with the wave-energy flux estimates in Section 6 and discuss the implications our results in Section 7.

2. OBSERVATIONS

To extend the previous work in Paper I, we use UV spectral diagnostics observed with the IRIS spacecraft to sample the upper chromospheric velocity and intensity diagnostics. For this paper, we concentrate in this paper on the Mn I 280.108 nm line (lower chromosphere, Pereira et al. 2013), the Mg II h₂ & k₂ features (middle chromosphere) and the Mg II h₃ & k₃ features (upper chromosphere, Leenaarts et al. 2013). The IRIS data archive offers a vast collection of observations containing this spectral line set. We compare the properties of the UV data with the results from Paper I to obtain new and more complete estimate for the energy fluxes that acoustic waves are carrying and the possible chromospheric heating implications.

Throughout the paper we will discuss two different types of solar features: *internetwork* and *plage*. These regions harbor weak magnetic fields in the case of internetwork and stronger magnetic fields in the case of the plage. The choice of these two types of solar surface is based on their relative simple discrimination from the rest of the solar structures. Furthermore, in the internetwork we didn't expect the weak magnetic field to be significant for the wave propagation. In the case of the plage, previous work showed the ubiquity of fluctuation signatures and a mostly vertical magnetic field (Pietrow et al. 2020; Anan et al. 2021), which could harbor MHD wave modes.

2.1. Processing of the IRIS data

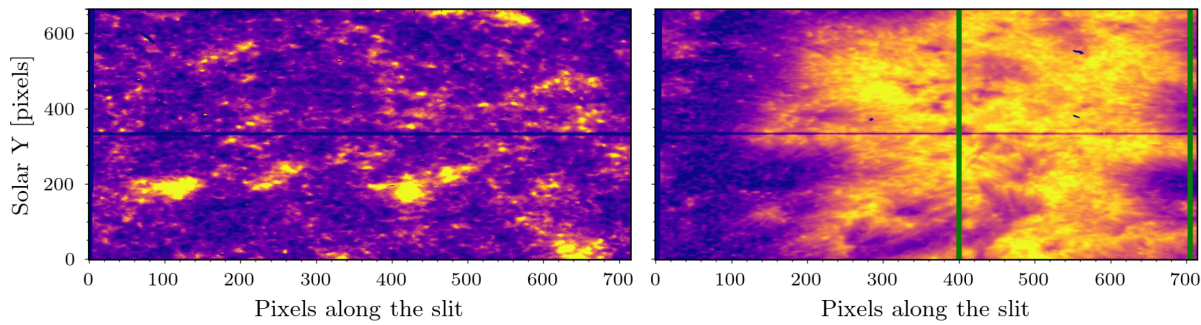
Date	Start [UT]	End [UT]	Cadence [s]	Solar feature
20131116	07:33	08:08	17.0	Internetwork
20140918	10:19	12:16	9.4	Plage

Table 1. IRIS observations used in this work.

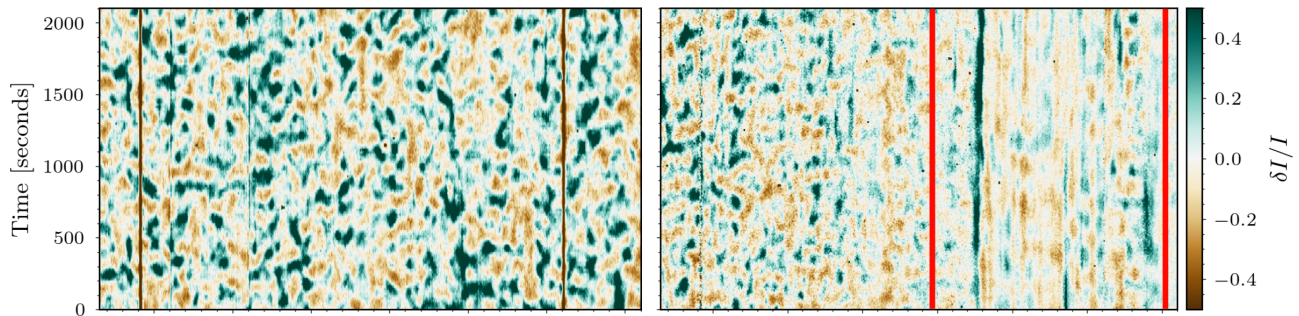
1. Internetwork

2. Plage

(a) SJI 279.6 nm



(b) Mn I 280.19 nm intensity



(c) Mn I 280.19 nm Doppler velocity

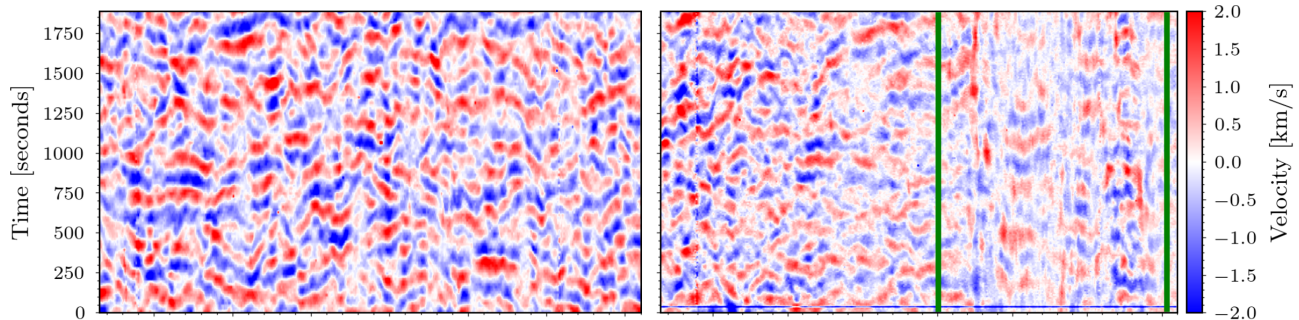
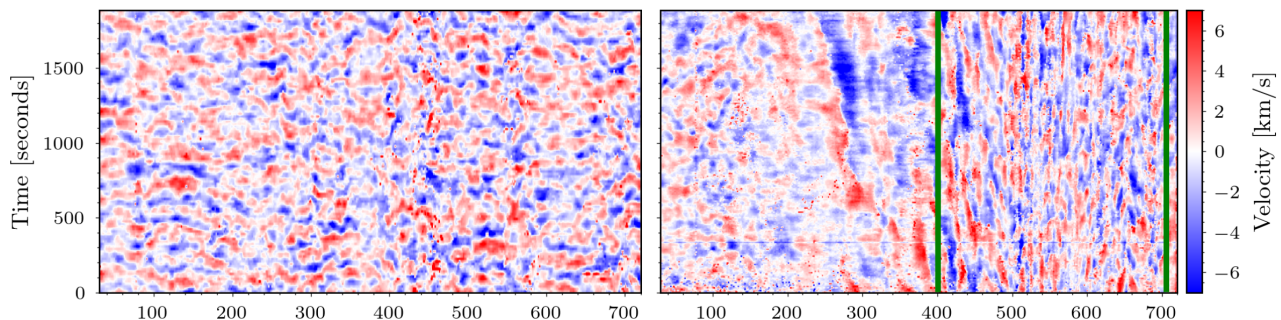
(d) Mg II k_3 Doppler velocity

Figure 1. The data used in this study comes from two different regions – internetwork (left column) and plage (right column), where the dark line across the center of the image is the actual slit. The left column shows observations of an internetwork region from 2013 November 16; the right column of a plage region observations from 2014 September 18 (see Table 2.1). The top row (a) are slit-jaw images in the 279.6 nm spectral window for the internetwork (left) and plage (right). Row (b) show the relative intensity variations (to the mean intensity at the particular slit position) at the core of the Mn I 280.19 nm line. Rows (c) and (d) show the Doppler velocities derived from the Mn I 280.19 nm line and the Mg II k_3 feature, respectively. All panels present along their x-axis the slit dimension.

We use the *level_2* spectral rasters from the IRIS online data archive¹ for this analysis. The particular datasets used in this study are described in Table 2.1. We chose two sets of observations from the earlier stages of the IRIS mission to ensure higher sensitivity and lower noise levels. The datasets used in this work are in sit-and-stare mode, which increases the signal-to-noise ratio of the observations and provides higher Nyquist sampling frequency.

The two UV spectral lines of interest have different shapes – the Mn I 280.1 nm line has a simple absorption profile, whereas the Mg II h & k lines have a complicated, typically double-peaked shape due to the high opacity non-equilibrium effects at chromospheric heights (Tousey 1967). We adopted different fitting approaches to extract the physical parameters from the two spectral lines. The Mg II h & k lines are fitted with the IDL routine *iris_get_mg_features_level2.pro*, part of the SSW IRIS reduction routine suite. This procedure relies on derivative estimates and subpixel interpolation to calculate the locations and amplitudes of the features of the Mg II h & k lines (described in detail in Pereira et al. 2013). In this work we concentrate our analysis on the properties of the k3 and h3 features, which are the central extrema (global maxima or a local minimum) of the line profile, that is always present, even in the plage region (Tousey 1967). The Mn I 280.1 nm line is situated between the Mg II k and h lines that produce a sloped background continuum. We used the IDL routine *gaussian_fit* to fit a combination of a Gaussian plus an inclined line on the wavelength range of ± 0.03 nm around the line center because the Mn I line has a regular absorption line shape. We derived the line properties from the parameters of the fitted Gaussian profile. Analysis of the Mn I 280.1 nm line and Mg II k feature formed the basis for the study by Kayshap et al. (2018), where the authors found clear signatures of wave propagation throughout the quiet solar atmosphere. The IRIS spacecraft pointing jitter during the sequences is negligible, verified by the cross correlation of individual slitjaw frames.

After deriving the fits of the spectral lines and calculating the resulting Doppler velocities and line-core intensities, we cleaned the data from non-converged line fits, which amounted to a few percent of the total fits. We first removed any non-converged fit values by replacing them with a 3×3 pixel median filter that excludes nearby non-converged fits pixels. We further smoothed out any discontinuities in the temporal domain in the velocity signal which are above the local sound speed

(7 km s^{-1}) with a 3×3 pixel median filter, which corresponds to a $0.5''\times 27$ seconds kernel for the plage and to a $0.5''\times 51$ second kernel for the internetwork. The Nyquist frequency of our data is 29 mHz for the internetwork and 51 mHz for the plage dataset. In the analysis in Section 3 we show that the frequencies containing valuable information are between 5 and 20 mHz, well below the Nyquist frequency. The spatial smoothing over $0.5''$ does not affect the estimated wave properties, as previous work utilizing high resolution data (e.g. Vecchio et al. 2007) has shown that the coherence scale of the velocity signals in the chromosphere is of similar spatial scale (see the bottom two rows of Figure 1). The resulting data products from the aforementioned reduction procedures are presented in Figure 1. The left column shows an internetwork region and the right one presents a plage region, both observed near to the disc center. Because the lower part of the plage field of dataset field of view is occupied by an internetwork, we exclude this part from the plage analysis. In particular, we use the slit locations between pixels 400 and 705, which are marked in the right column of Figure 1 as the green (red) lines. For the internetwork, we use the full extent of the slit.

2.2. Processing of the IBIS data

This study uses data from the Interferometric BIdimensional spectrograph (IBIS, Cavallini 2006) instrument acquired during the ALMA coordinated observing campaign on 2017 April 23. The observed region was centered on the leading edge of AR 12653. The FOV was $96''$ and included regions of plage, internetwork, network and penumbra. These observations were taken between 17:25-18:12 UT and include scans of the Na I D₁ 589.6 nm and the Ca II 854.2 nm line, consisting of 24 and 27 points in each line respectively, which were described in detail in Hofmann et al. (2022). This data series has a temporal cadence of 16 sec and spectral resolution of at least $R \gtrsim 200,000$ (Reardon & Cavallini 2008). The line cores were more densely sampled than the wings of the spectral lines because the core region is used for deriving the quantities used in this study (Doppler velocities and line-core intensities). The IBIS data processing is described in detail in Molnar et al. (2019), where we have applied the standard reduction techniques of removing instrumental and atmospheric image aberrations and de-stretching the resulting data to the HMI whitelight (atmospheric seeing-free) reference. In this work we use the datasets starting at 15:54 UT and 16:37 UT, which were taken under conditions of good seeing.

3. PROPERTIES OF THE OBSERVED POWER SPECTRA

¹ <https://iris.lmsal.com/data.html>

We studied the wave dynamics in the observed chromospheric diagnostics by analyzing their power spectra. The power spectra are derived for each pixel in the selected interval along the slit from the squared absolute value of the Fourier transform of the time series, giving us the power spectral density (PSD) of the data. The power spectra of the IRIS data exhibit ubiquitous power law shapes at frequencies above the acoustic cutoff present in all chromospheric and photospheric observables. These power laws exhibit similar behavior to those previously observed in the chromosphere, for example in Reardon et al. (2008) and will be further discussed further below. The average shapes, slopes and other properties of the power laws are presented in this section.

Solar Feature Spectral line	Slope	Noise floor [(km/s) ² /mHz]	$\langle v^2 \rangle$ [(km/s) ²]
IN Mn I	$-3.56^{+1.02}_{-0.89}$	$3.2^{+2.1}_{-1.3} 10^{-4}$	$0.18^{+0.12}_{-0.065}$
IN Mg II k3	$-2.33^{+0.85}_{-0.91}$	$1.1^{+1.7}_{-0.5} 10^{-2}$	$1.76^{+0.97}_{-0.55}$
Plage Mn I	$-3.09^{+0.88}_{-0.81}$	$4.0^{+0.9}_{-0.6} 10^{-4}$	$0.02^{+0.03}_{-0.005}$
Plage Mg II k3	$-1.22^{+0.90}_{-0.86}$	$1.7^{+0.9}_{-0.6} 10^{-2}$	$2.31^{+1.18}_{-0.98}$

Table 2. Average PSD properties of the observed solar regions in the two IRIS lines (Mn I 280.1 nm and Mg II k3) with the 10th/90th percentile quoted. The amount of oscillatory velocity power is calculated between 5 and 20 mHz with the white noise subtracted. The calculation of the properties is described in detail Section 3.

Figure 2 presents the average power spectral profiles (PSDs) and their derived properties for the different solar regions and spectral diagnostics. The average power spectra for the different solar regions are shown in the top panel. The internetwork data exhibits the typical 3 minute (5 mHz) peak in both the Mn I line (lower chromosphere) and the Mg II k line (upper chromosphere). This can be seen clearly from the last two rows of Figure 1, where the velocity diagnostics of the quiet sun exhibit regular pattern with the time scale of about 3 minutes. The plage data exhibits a peak at lower frequencies, around the 3 mHz (5 minute) oscillations (as previously shown by de Pontieu 2004; Morosin et al. 2022; Sadeghi & Tavabi 2022), which is more pronounced for the lower chromospheric diagnostics. Furthermore, the Doppler velocity observations in the plage (last two rows of Figure 1) do not seem to exhibit the clear oscillatory pattern seen in the internetwork data, which results in a less well defined peak in their Doppler velocity power spectra.

Zaqarashvili & Skhirtladze (2008) have suggested that the lower frequency peak in the velocity PSD in the

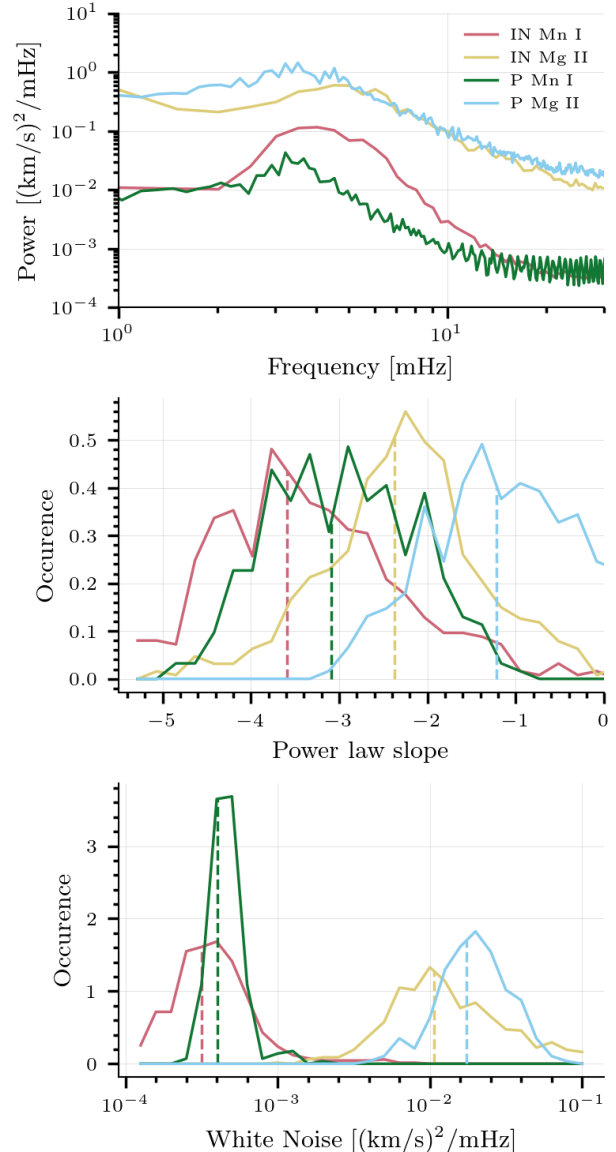


Figure 2. Observed power spectra and their power law properties for the different solar regions and spectral diagnostic. *Top Panel:* Average power spectra. *Middle Panel:* Histograms of the slopes of the fitted power laws. *Bottom Panel:* Histogram of the white noise floors for the different diagnostics. The color coding is consistent throughout the paper. The analysis of the data presented in this figure are described in detail in Section 3.

plage regions might be a signature of the kink wave frequency in the chromosphere. However, we did not find a clear correlation between the cotemporal magnetic field strength in the photosphere measured by SDO/HMI (Schou et al. 2012) and the peak of the plage velocity PSD, as suggested from the behavior of the kink-wave cutoff. We intend to extend this study to look for the signatures of the kink-wave cutoff frequency complemented with chromospheric magnetic field measurements from

DKIST (Rimmele et al. 2020) combined with IRIS observations in a following publication.

To quantify the usable range of frequencies for our analysis we calculated the white noise floor, that is clearly seen in Figure 2 Panel (a) as the flat, frequency-independent signal at high frequencies. We compute the white noise floor as the median power above 25 mHz frequency. This noise-frequency cutoff is outside of the frequency range used for the wave-power analysis. The white noise floor distributions of the different solar regions are shown in the Figure 2 Panel (c). Similarly to the results in Paper I, we observed that the white-noise floor is slightly higher for the plage when compared with the internetwork regions. We also found that the Mg II-derived diagnostics have a higher white noise floor compared with the Mn I ones. This trend might be due to the measurement technique and/or the nature of the chromospheric lines in question, as the Mg II lines have a complex shape that requires an elaborate fitting routine (Pereira et al. 2013). By examining the mean frequency when power rises above the white noise level, we defined the meaningful frequency region of the PSDs to be used for further analysis to be 20 mHz for internetwork regions and 12 mHz for the plage regions, because white noise dominates above those frequencies, as clearly seen in panel (a) of Figure 2.

We perform linear fit on the log-log representation of the velocity PSDs to estimate the power law slopes. The middle panel of Figure 2 presents the power law slopes of the observed PSDs for the different regions of interest. For the plage regions we fit the data between 3 and 12 mHz, and for the quiet Sun we fit the interval between 5 and 20 mHz, due to the different levels of white noise, discussed in the previous paragraph. The dotted lines show the median of the power law slope distributions. The power laws of the diagnostics formed in the lower chromosphere exhibit steeper slopes compared to the ones formed in the upper chromosphere. Interestingly, for both IRIS lines the plage exhibits steeper power law slopes than the internetwork regions, similarly to the behavior of the Ca II IR line in Paper I. The slopes of the vertical velocity PSDs are signatures of the wave environment in the chromosphere and they are a crucial dynamic constraint for realistic rMHD models of the solar chromosphere.

Figure 3 shows the integrated Doppler velocity oscillatory power between 5 and 20 mHz in the Mn I and the Mg II k₃ features as the blue distributions. We analyzed only these frequencies, because waves with these periodicities, above the acoustic cutoff frequency (about 5 mHz in the solar photosphere), will be able to propagate upward. The acoustic cutoff frequency varies across the so-

lar atmosphere (Felipe et al. 2018; Jefferies et al. 2019), being lowered at locations with strong magnetic field concentrations (Hegglund et al. 2011), but our choice to exclude the power between 3 and 5 mHz is a conservative estimate of the wave flux, which will not change the end result by more than a factor of about two, which is not enough to change the conclusions of this work, as shown in Section 6. We also degraded the resolution of the synthetic data down to the resolution of the IRIS and IBIS instruments to take into account their diffraction limits.

We also included the amount of oscillatory power from the optical lines of Na I D₁ and Ca II 854.2 nm observed with IBIS. In all cases, for both IRIS and IBIS diagnostics, we have subtracted a local estimate of the high-frequency white noise component for each pixel, following the noise estimation procedure described in the previous paragraph. Those IBIS observations were obtained on a different day and region than the IRIS data analyzed here, but we applied feature-selection criteria described in Paper I, making for a suitable statistical comparison between these diagnostics. In Figure 3 the blue distributions are derived from observations, and the green ones from simulations, which will be described in Section 4.2. The average values of the IRIS velocity fluctuation power are summarized in Table 2.

An increase in the amount of velocity oscillatory power is observed with increasing height in the observations in Figure 3, where the spectral diagnostics are arranged in order of increasing height of formation. This is presumably due to the steeply decreasing density with height in the solar atmosphere, leading to increasing wave amplitudes, even though the actual wave flux maybe decreasing with height. We also note that the absolute amount of observed line-of-sight velocity oscillations is higher in the internetwork in the lower chromosphere compared with the plage regions. However, in the middle and upper chromosphere the difference in the amount of velocity oscillation between the internetwork and the plage almost diminishes.

The Na I D₁ line velocity data agree well with the velocity data from the Mn I 280.1 nm line, which is unsurprising given that both lines are formed at similar heights on average (Leenaarts et al. 2010; Pereira et al. 2013). The Ca II 854.2 nm line shows velocity fluctuation amplitudes between the Mn I and Mg II k₃ feature. This confirms that the resulting wave amplitudes, coming from different spectral lines is self-consistent and presents a uniform physical picture of the amount of wave amplitude in the solar atmosphere.

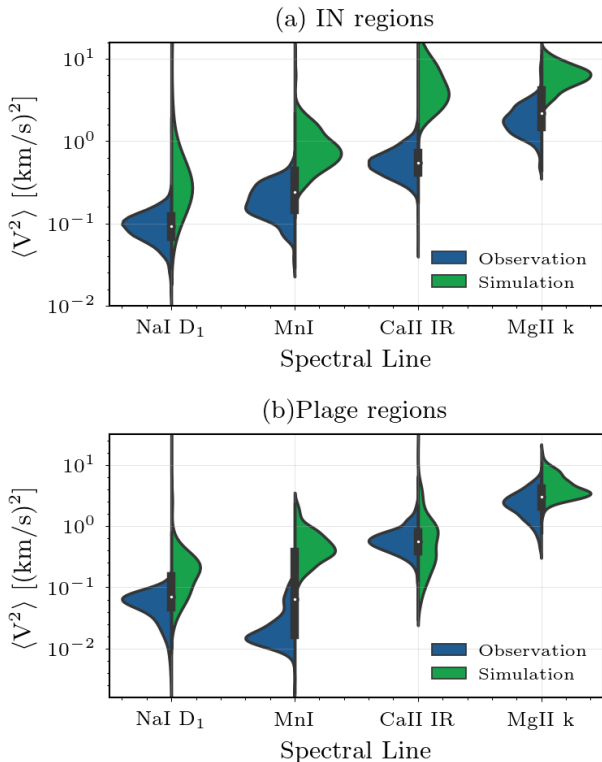


Figure 3. Integrated Doppler velocity oscillation power between 5 and 20 mHz in the IRIS and IBIS diagnostics in the two different solar features (see Section 3), after subtraction of the white noise floor. The ordering of the spectral lines reflects their relative average height of formation in the solar atmosphere. The blue distributions are real observations, whereas the green distributions are Bifrost-derived synthetic observables.

4. ACOUSTIC WAVE PROPAGATION IN SOLAR SIMULATIONS: 1D VS 3D MODELS

The energy flux F_{ac} of propagating acoustic waves with frequencies between ν_{ac} (the acoustic cutoff frequency) and an upper-limit frequency ν_1 can be derived from observations with the following expression (following the derivation in Bray & Loughhead 1974; Bello González et al. 2009):

$$F_{ac} = \rho \sum_{\nu'=\nu_{ac}}^{\nu_1} \frac{\langle v_{obs}^2(\nu') \rangle}{\mathcal{T}^2(\nu')} v_{gr}(\nu') \quad (1)$$

where ρ is the plasma density at the formation height of the observed diagnostic; $\langle v_{obs}^2(\nu') \rangle$ is the observed velocity variance at frequency bin ν' ; $\mathcal{T}(\nu')$ is the attenuation coefficient due to the finite thickness of the formation region of the spectral line (Mein & Mein 1976); $v_{gr}(\nu')$ is the group velocity of the wave mode at frequency ν' . To estimate the wave energy flux, we have to evaluate the terms on the right side of Equation 1 from models or observations. The quantity $\langle v_{obs}^2(\nu') \rangle$

can be obtained from the observations as described in Section 2. The other three quantities however need to be estimated from numerical models, as we describe in this Section.

We extend previous analyses (Fossum & Carlsson 2005; Wunnenberg et al. 2002; Sobotka et al. 2016) to compare the differences between 1D models (FAL, RADYN) and 3D models (Bifrost). In comparison with 1D models, the Bifrost model includes additional physical processes (dynamical evolution, shock formation, detailed radiative transfer and non-equilibrium ionization of hydrogen) which produce a wealth of small-scale phenomena. This approach allows for self-consistent description of wave propagation in the chromosphere, avoiding some of the problems with 1D modeling described in Ulmschneider et al. (2005). Previous work by Fleck et al. (2021) compared the general wave propagation properties in 3D MHD simulations, including Bifrost, and found a lack of general agreement among the different models. We note that those authors did not explore the observational signatures of high-frequency wave propagation in the chromosphere, which is the central topic of this paper.

4.1. RADYN models

We use the same RADYN (Carlsson & Stein 1992; Allred et al. 2005, 2015) runs presented in Paper I to interpret the IRIS observations. The initial RADYN atmospheric model used was an IN atmosphere model with 191 grid points. The model has a piston-like lower boundary condition that acts as a sub-photospheric wave driver and an open upper boundary with constant temperature of 1 MK. RADYN self-consistently solves the equations of radiative transfer, statistical equilibrium, and the hydrodynamic equations, where the code can take into account the time dependent ionization. Furthermore, the RADYN code treats in non-LTE the transitions of hydrogen, calcium, and helium with 6, 6, and 9 level atom models respectively.

We synthesized time series of spectral line profiles from these models. Based on these synthetic observables, we estimated the line displacements and intensities described in the further analysis. To synthesize the Mn I, and the Mg II spectral diagnostics studied throughout this work, we use the RH 1.5D code (Uitenbroek 2001; Pereira & Uitenbroek 2015). For the synthesis of the Mn I 280.1 nm line, we used the Kurucz line list database² (Kurucz 2018) and we synthesized it in local thermodynamic equilibrium (LTE). We note that the lines of Mn I exhibit non-LTE effects (Bergemann

² <http://kurucz.harvard.edu/linelists.html>

et al. 2019), but we leave the assessment of importance of these effects for a future work. To synthesize the Mg II h & k lines we used the RH code in non-LTE mode with 10 plus one Mg III ground levels and PRD treatment (the same setup used in Leenaarts et al. 2012).

4.2. Bifrost models

Modern 3D radiative magnetohydrodynamic (rMHD) codes appear to result in increasing levels of realism of the simulated solar atmosphere (Björge et al. 2019). To leverage the advantages of multidimensional rMHD simulations, we use the publicly available Bifrost **data cubes**³ of enhanced network *en024048_hion* (Gudiksen et al. 2011; Carlsson et al. 2016). In this simulation we utilize the quiet regions as realizations of quiet Sun internetwork and the more active network as representative of plage regions. We further employed the publicly available radiative transfer products for the Mg II h & k and the Mn I 280.9 nm lines which are synthesized with the RH 1.5D code and publicly available for the enhanced network *en024048_hion* (Pereira et al. 2013). We also synthesized the Ca II 854.2 nm and Na I D₁ lines with RH 1.5D in nLTE. We used a 6-level model atom for the Ca II 854.2 nm line, including a Ca III ground state; for the Na I D₁ line, we used a model atom with 4 levels which includes a Na II ground state.

Before proceeding with the analysis of the spectral synthesis products, we note a few deficiencies of the Bifrost models, which should be kept in mind while interpreting the following results. First, the UV solar spectrum is not well reproduced, with spectral features lacking in intensity and width (Pereira et al. 2013). As discussed previously in Carlsson et al. (2016), this might be due to a combination of factors, like insufficient heating in the chromosphere and corona and the lack of small-scale motions in the simulated atmospheres. The other major drawback of these models is the presence of global oscillations over the whole simulation domain with velocity perturbations on the order of a few km/s in the lower chromosphere, accompanied by density fluctuations on the order of 20 percent (described previously in Carlsson et al. 2016; Fleck et al. 2021). We have attempted to remove the signature of these wave modes in our analysis by filtering them in temporal Fourier space, given their periods are lower (about ten minutes) compared with the periods of interest in this paper and are coherent over the whole domain.

4.3. Properties of the synthetic observables from Bifrost

Figure 4 shows the formation properties of the Mn I 280.1 nm line (top panel) and Mg II k3 (middle panel) in the enhanced network Bifrost simulation. Panels (a) and (e) show the height of optical depth unity, referred to as the *height of formation* of the spectral line. These panels indicate that the two spectral lines are formed at significantly varying heights in the atmosphere at different locations in the FOV, as previously shown in Pereira et al. (2013). This spread of the height of formation is a significant contribution to the broad distribution of densities at the $\tau=1$ heights, which are shown in Panels (b) and (f). This raises the question of the applicability of the approach based on inferring the acoustic flux using a singular density value for a given spectral line. Additionally, the effective height of formation of a spectral line may change as the atmospheric properties evolve in time. The amplitude of this effect is illustrated in panels (c) and (g) which show for each line the ratio of the difference between the 10th and 90th percentile of the temporal density variation to the time-averaged plasma density at the height of formation for each pixel. We note a strong temporal variation of the density at the height of formation with time on the order of a factor of few for the same temporal location, similarly to Felipe et al. (2023). This change is due to the passing wave fronts and the different amplitudes are due to the significantly different properties of formation of the diagnostics in the two regions. For the Mn I line, the density of formation changes by an order of magnitude in internetwork regions over time, but relatively less in the enhanced network regions. For the Mg II k line, we see that the density changes most significantly along the fibrillar structures, connecting the two magnetic regions in the simulation domain.

Based on the spectral synthesis of the two UV and the two optical lines, we computed $\tau=1$ plasma density histograms for each spectral line from the first snapshot of the simulation. Panel (i) shows that the densities at the $\tau=1$ heights exhibit wide distributions that present a challenge for the computation of the wave fluxes. If we examine indicative enhanced network (magenta squares in Panels (a) and (e)) and internetwork (green squares in Panels (a) and (e)) structures we find that those regions exhibit almost constant density inside the small boxes. The average of the density from those regions could be used as the representative of the values to be used in Equation 1 when estimating the acoustic fluxes. This strong dependency of the density on the particular solar region, further described in Section 5, makes providing an accurate model for every solar feature crucial for the accurate estimation of the wave flux.

³ Available at <http://sdc.uio.no/search/simulations>.

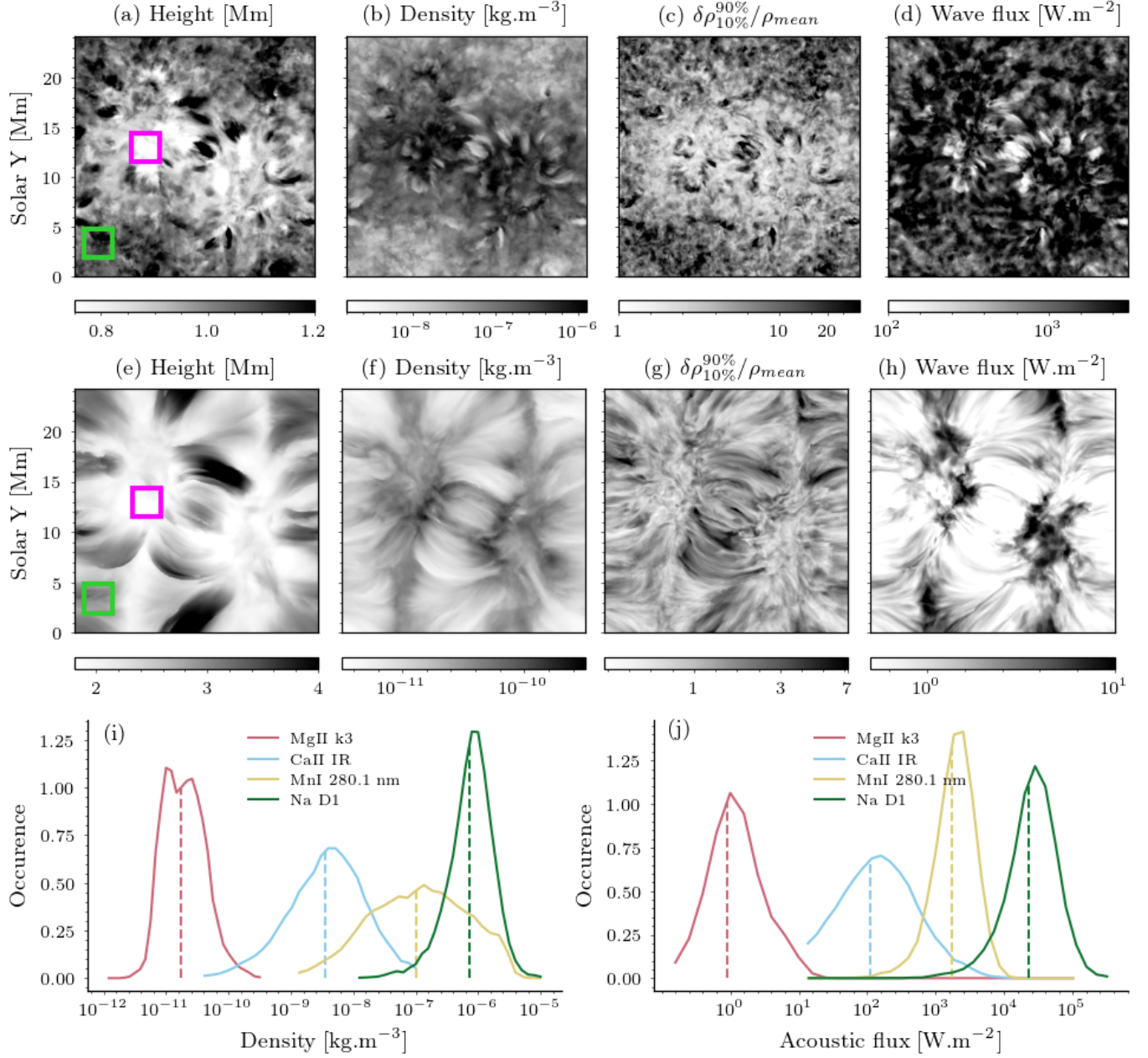


Figure 4. Results from the Bifrost spectral synthesis. The top row shows diagnostics derived from the Mn I 280.1 nm line and the middle row shows those for the Mg II k3 feature. Panels (a) and (e) show the time-averaged height of optical depth unity of the line core, panels (b) and (f) the time-averaged density at optical depth unity for the line core; panels (c) and (g) show the ratio of the plasma density change over time to the mean plasma density at the formation height of the spectral lines, and panels (d) and (h) the acoustic flux at the formation height of the spectral line. The green and magenta squares in panels (a) and (e) are the representative regions that we equate to internetwork and plage regions in our observables in the following analysis. The bottom left panel (i) shows the distributions of the density at the height of formation in the simulation for the different diagnostics; the bottom right panel (j) shows the distributions of the acoustic flux at the height of formation of the diagnostics.

The acoustic wave flux present in the simulation cube can be computed at different heights as the plasma conditions are known. Due to the varying formation conditions of the diagnostics, described in the previous paragraph, we estimated the average height of formation for each spectral line separately for each column of the simulation. Based on the average height of the column, we extracted the average plasma density and the amount of vertical velocity oscillatory power between 5 and 20 mHz at that height in the simulation. Based on these estimates, we computed the average wave flux at the local formation height of the spectral lines. The resulting acoustic wave-flux distributions for all spectral lines are presented in Panel (j) of Figure 4. The amount of acoustic flux with height decreases significantly, in contrast to the almost constant amount of wave flux in the 1D RADYN chromosphere (Fossum & Carlsson 2006). This is the typically observed behavior of the wave flux with height, as hinted by previous observations (e.g., Abbasvand et al. 2020b). The amount of acoustic wave flux in the Bifrost simulation chromosphere resembles the results based on the RADYN models in Paper I, but exhibit a more realistic decrease of the wave flux with height (Ulmschneider et al. 2005). This is further described in detail in Section 4.3.

Based on the spectral profiles computed from the Bifrost simulation, we measured the Doppler velocities using the same procedure as for the real observations, described in Section 2.1. We have also subtracted a white-noise estimate, derived as frequency independent at high frequencies of the power spectrum. We compare the amounts of Doppler velocity fluctuations in the real data (blue distributions) and the simulations (green distributions) in Figure 3. The data for the simulation results are based on the aforementioned green and pink regions in Figure 4. The simulations seem to exhibit significantly higher velocity oscillation power than the actual Sun, often up to a magnitude more.

The acoustic wave energy propagating through the chromosphere appears to be mostly dissipated by the time it reaches the height of formation of the Mg II k3 feature (see Figure 4 Panel (h)). in the simulations. This is further illustrated in Figure 5, where the height dependence of the acoustic flux in the internetwork and magnetic concentration regions are shown. The amount of velocity variance is also shown in Figure 5 as the dashed lines. We can see that the amounts of vertical velocity oscillatory power in the internetwork and the plage are similar in the photosphere, but in the chromosphere the internetwork has higher velocity oscillation power by a factor of two. However, when taking into account the slightly lower density at chromospheric heights for the

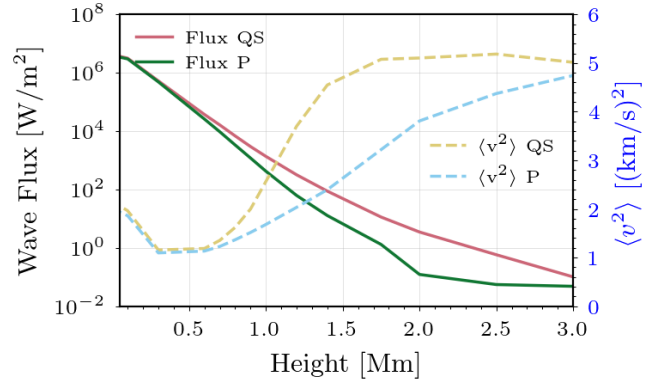


Figure 5. Height variation of the acoustic flux and vertical velocity fluctuation amplitude between 5 and 20 mHz in the Bifrost model for internetwork (green) and plage regions (red). The solid (dotted) lines show the wave flux (velocity fluctuation). The regions of the simulation used are shown in Panels (a) and (e) of Figure 4 as the colored squares.

internetwork, compared with the enhanced network, we found that the velocity amplitudes are almost the same over a large range of heights.

This analysis shows the drawbacks of using 1D atmospheric models to infer the wave fluxes. First and foremost, perturbative approaches (such as Bello González et al. 2009; Abbasvand et al. 2020b) cannot account for the atmospheric properties changing significantly between different solar features. There has been previous work by Fossum & Carlsson (2005, 2006) that used time-dependent 1D HD RADYN models to infer wave fluxes from the TRACE observations, but these authors did not use differing starting atmospheric models to study the behavior of different solar features; or have used multiple 1D semi-empirical static models (Sobotka et al. 2016). Furthermore, the analysis of the 3D models shows that the high-frequency waves do not oversaturate the chromosphere with acoustic power as in the 1D case (Ulmschneider et al. 2005).

A key property that affects the estimation of the acoustic flux is the plasma density. We do not argue about the veracity of the conclusions in either approach, as the reliability of 3D models to represent the wave dynamics of the solar atmosphere is still under debate (Fleck et al. 2021). Furthermore, the too-weak spectral lines in the synthetic spectra are most probably due to low densities in the Bifrost simulations (Carlsson et al. 2016). In the next section, we compare the different modeling approaches, quantifying their systematic differences, which might explain some of the discrepancies among the previous results for acoustic flux estimates.

5. SYSTEMATICS OF ACOUSTIC WAVE FLUX ESTIMATION FROM 3D VS 1D MODELS

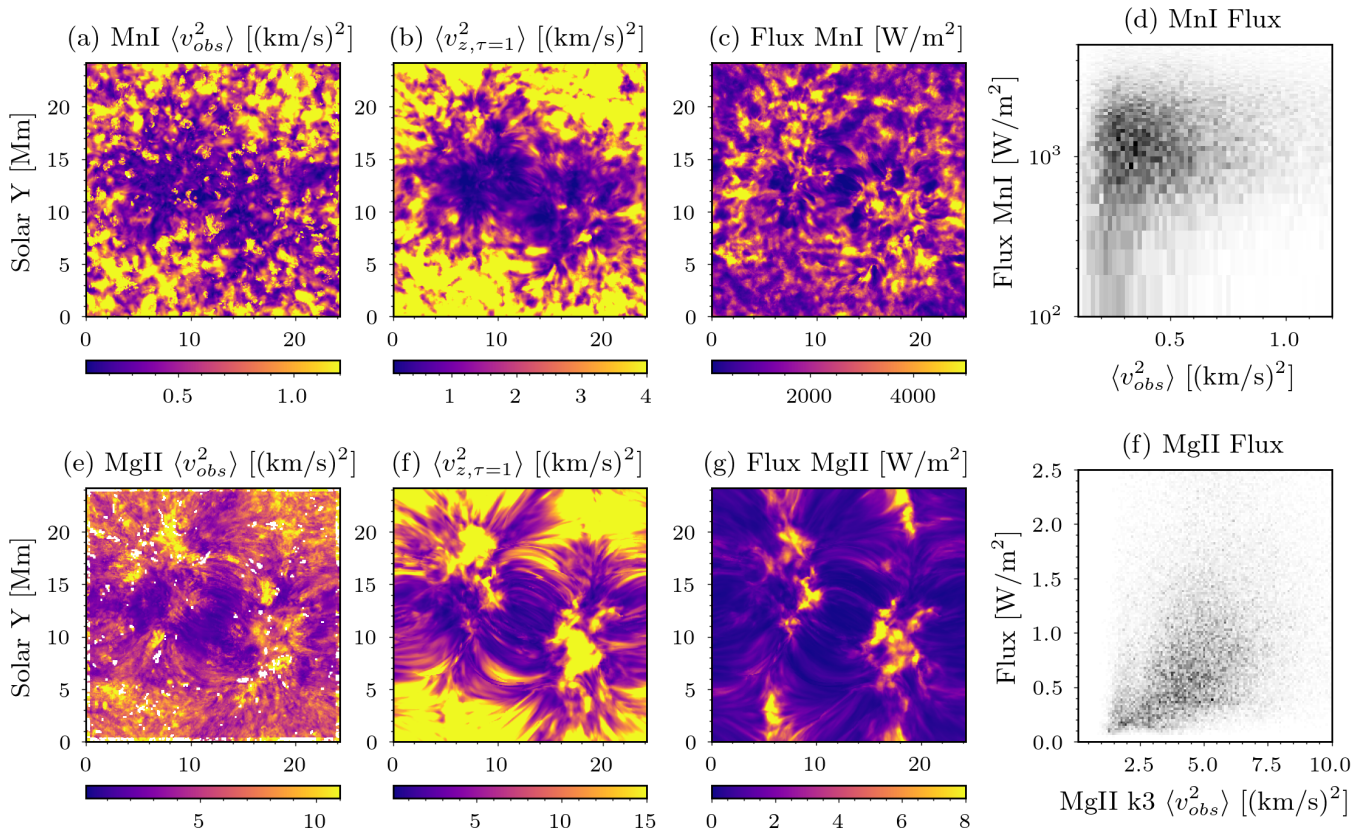


Figure 6. Comparison of the synthetic Doppler velocity fluctuations in the Mn I line and Mg II k3 feature and the wave fluxes at the corresponding heights in the model atmospheres. The top presents the following Mn I 280.1 nm derived diagnostics: panel (a) shows the measured synthetic Doppler velocity fluctuations between 5 and 25 mHz; panel (b) shows the vertical velocity oscillatory power between 5 and 25 mHz in the Bifrost simulation at the $\tau = 1$ height for each column; panel (c) shows the acoustic flux as measured in the simulation at the $\tau = 1$ height for each column, and panel (d) shows the scatter plot between the quantities in (a) and (c). The bottom row shows the same features, but for the Mg II k3.

The spectral synthesis of observables from numerical solar models provides us with a direct way to examine how the variations in measured diagnostics relate to the actual changes in atmospheric plasma properties. In this section we examine the behavior of the following components of Equation 1 in different modeling approaches: (i) atmospheric velocity at height corresponding to the observed Doppler velocity measurement and what is the source of the observed velocity fluctuations – true plasma motions or rather changes in the $\tau=1$ surface; (ii) what is the density at the height of formation associated with the oscillatory signal; and (iii) what is the transmission coefficient in different regions of the solar atmosphere. We compare the results from the 3D Bifrost simulations with previous results from RADYN and FAL atmosphere-based modeling (Fontenla et al. 2011). Such comparison allows for estimating the systematic errors that are introduced by using a particular modeling approach. This is an important aspect of these studies that has not been well constrained previously. We demonstrate that specific choices made for

the height of formation, density, and transmission coefficient can drastically change the conclusions from these of studies.

5.1. Measuring velocity fluctuations, but where?

The analysis in Section 4.3 shows that the Doppler velocity signals derived from synthetic spectral lines originate from a height that can change with time and depending on the underlying solar feature. Hence, we need to determine at which height the Doppler velocity samples the true vertical velocity field most closely.

To constrain to which height the observed Doppler velocity relates to, we calculated the Pearson correlation coefficient between the observed Doppler velocity and the plasma vertical velocity. The highest correlation coefficient values were found at the heights of the time-averaged optical depth unity which confirmed our previous calculations.

We compared the Doppler velocities in the synthetic spectral observations with the acoustic flux at the $\tau = 1$ height of formation of the spectral line. The results are

shown in Figure 6, where the first row is for the Mn I line and the second row is the Mg II k3 feature. Optimally, there would be a direct mapping between v_{obs}^2 and the wave energy flux, which would imply that the estimation of the density and the attenuation coefficient should be straightforward.

For both spectral lines, there is a good agreement between the distribution of the observed synthetic velocity oscillations and the true vertical velocity oscillations at the line height of formation in the solar atmosphere. Panels (a) and (b) of Figure 6 show the observed Doppler velocity and the velocity at the time-averaged $\tau=1$ height for the Mn I 280.1 nm line. Panels (e) and (f) show the same for the Mg II k3 feature. On average the observed Doppler velocity fluctuations are lower than the true vertical plasma velocities in the solar atmosphere. This is due to a Doppler velocity attenuation effect that smears out the vertical velocity signal in the solar atmosphere. It is caused by a combination of multiple phases of the acoustic waves might be present in the width of the formation region as well as the changing line height of formation (Mein & Mein 1976). This observed decrease of the wave amplitudes is described by the \mathcal{T} coefficient, discussed further in Section 5.3. The total amplitudes of the velocities derived from the synthetic observables are on average lower by a factor of two to four, due to the attenuation of the signal.

However, when we compute the acoustic fluxes at the time-averaged $\tau = 1$ surfaces of the simulations, we see that the correspondence with the velocity amplitudes is mostly nonexistent (panels (c) and (g)). This is due to the fact that the other major component of the acoustic flux calculation is the density. The density at the height of line formation varies significantly in the different regions of the chromosphere, as shown in panels (b) and (f) in Figure 4. In particular, these subfigures show us that the local density changes by more than an order of magnitude between the quiet and enhanced network regions. This can be understood as in the hotter (network) regions, the diagnostics are formed at a lower height and on average at higher column mass (Fontenla et al. 2011). The density variation is significantly higher than the variation of the amplitudes of the observed velocity fluctuations in the simulations.

This strong spatial variation of plasma properties results in the poor correlation between the observed synthetic velocity oscillation power and the acoustic flux at the line formation region, as shown in panels (d) and (f) of Figure 6. The correlation is marginally better for the case of the Mg II k3 feature. The relatively smaller change of the density of formation in the case of the upper chromospheric Mg II k3 leads to a better correlation

between the synthetic observed velocity fluctuations and the acoustic flux in the atmosphere.

The conclusion from Figure 6 is that the variations in the formation height of the spectral lines in different features is a significant effect when estimating the wave flux in the solar atmosphere, as that will alter the observed wave velocity amplitudes and local densities. Using fixed values for the density will produce results that do not correspond to the true flux at the formation region of the spectral lines. Optimally, we would take this into account when estimating the acoustic flux by employing different densities. However, as we discuss in the following section, sufficient knowledge of the local densities in the chromosphere and their range of variation, is still lacking.

5.2. Chromospheric density estimates are model dependent

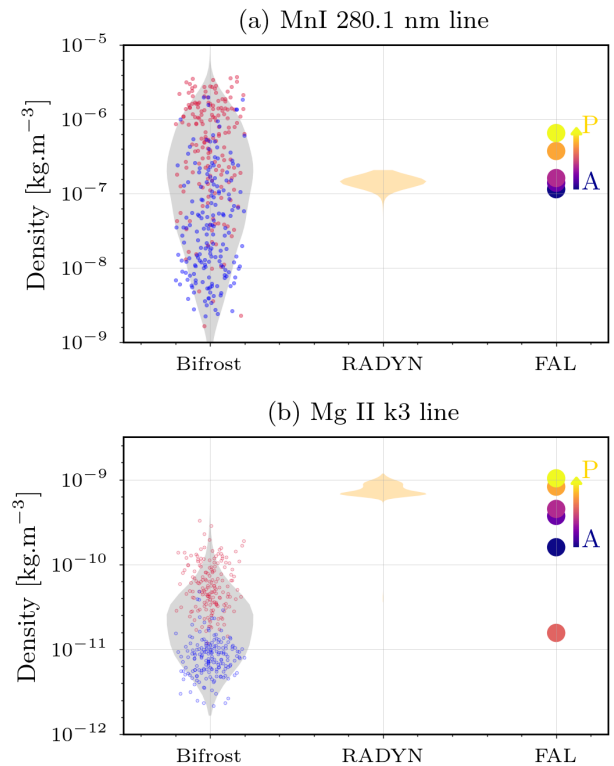


Figure 7. Density at the line formation height for the Mn I 280.1 nm line and the Mg II k3 feature from different wave modeling approaches labeled on the abscissa. The top panel (a) shows the results for the Mn I line and the bottom panel (b) for the Mg II k3 feature. The data points overlaying the Bifrost density distribution correspond to internetwork (blue) and enhanced network (red) regions shown in Figure 4 sampled every 200 seconds.

Density is the quantity with the highest degree of variability in estimating the acoustic flux in the chromosphere, due to its highly corrugated and dynamic structure (Carlsson et al. 2019). As alluded in the previous subsection, the density at the formation location of the same diagnostics in different regions of the solar atmosphere changes by a few orders of magnitude, as illustrated in panels (b) and (f) in Figure 4. In this section we discuss the intrinsic variability of the plasma density at the height of spectral line formation in the different modeling approaches. The variability described here is due to the different line formation conditions in the model atmospheres, not the intrinsic changes due to the wave perturbations per se.

Figure 7 shows the distribution of plasma densities at the $\tau = 1$ surface for the Mn I 280.1 nm line in panel (a) and the Mg II k3 feature in panel (b) for different modeling approaches. The three different models described here are: Bifrost 3D rMHD simulations described in Section 4.2; the RADYN models described in Section 4.1; and the FAL11 semi-empirical 1D hydrostatic models, described in Fontenla et al. (2011). We use the latest FAL models, since they reproduce the average solar spectra to the best extent, but are in essence very similar to other 1D semi-empirical atmospheric models used in previous acoustic wave studies.

For the Bifrost rMHD model, we extracted the corresponding densities at every 5th spatial pixel in both spatial dimensions at 200 second intervals. The distribution of the Bifrost densities are presented as the gray distribution in Figure 7. We also calculated the densities at the two regions of internetwork and active network, marked as the squares in Figure 4. We plotted them over the full Bifrost distribution with the blue (internetwork) and red (active network) markers. The formation of the lines in the active network is at higher average plasma densities, which agrees with the previous discussion in Section 4. For the RADYN models, we calculated the Mn I and the Mg II lines for the *model_3000* run from Paper I for every temporal step, where we have excluded from the synthesis the relaxation time of the simulation. We calculated the density from the other models presented in Paper I that have increasing wave strength, but the results were similar to the ones presented here. The FAL models A-P, increasing in activity from very quiet internetwork to plage core, are shown with the colored circles on the right. The relative warmth of the color of the marker signifies increasing activity level.

The different modeling approaches produce very different estimates for the plasma density at the line formation region, as shown in Figure 7. In particular, the Bifrost models exhibit a high level of intrinsic variation

of the density in the different solar features. In the case of the Mn I line, the RADYN-derived density corresponds to the quietest FAL models, which is not surprising, given the initial RADYN atmosphere was based on a relaxed FAL B like model. Comparing the Bifrost density estimates with the 1D model ones, we observed that mostly the active network regions have mostly similar density to the ones retrieved from the FAL-based modeling. In the internetwork, the Bifrost models estimated that the density of formation is significantly lower than the one derived from the FAL models, but at some points they exhibit high densities, similar to the ones seen in the enhanced network.

In the case of the Mg II lines, the RADYN models exhibit densities closer to those of the hotter FAL models, opposite from what is seen in the Mn I 280.1 nm line case. However, the more self-consistent Bifrost simulation exhibits significantly lower density than either FAL and RADYN simulations for both enhanced network and internetwork.

Using the values of Bifrost simulation-derived densities for flux estimates would lead to lower inferred chromospheric wave fluxes when compared with using values based on the FAL models. We do not dispute which density values are more accurate, as the Bifrost models still lack heating and sufficient density in the chromosphere to properly reproduce the observed spectral profiles. Instead, we highlighted the systematic biases in different wave flux estimates based on the models used. The large spatial and temporal spread in densities in the more dynamic rMHD models does further indicate the use of a single or few values of density in computing wave fluxes is likely an oversimplification that leads to significant uncertainties.

5.3. Uncertainty of the transmission coefficient

The attenuation coefficient \mathcal{T} is the last model-dependent parameter in estimating the wave flux. We define \mathcal{T} in this work as the ratio of the standard deviation of the observed and actual atmospheric vertical velocities. We take a frequency-averaged approach, as previous work in Paper I calculated \mathcal{T} as a function of frequency and showed that most of the power is at the lower frequencies. To examine its variation in the Bifrost simulations, we calculated the ratio of the standard deviations of the Doppler velocities, derived from the synthetic observations, and the vertical velocities in the simulation at the time-averaged height of the $\tau = 1$ surface. We have filtered the vertical velocities in Fourier space leaving the frequencies between 5 and 20 mHz. We adopt an averaging of the velocity fluctuation power over the frequency domain for calculating \mathcal{T} , dif-

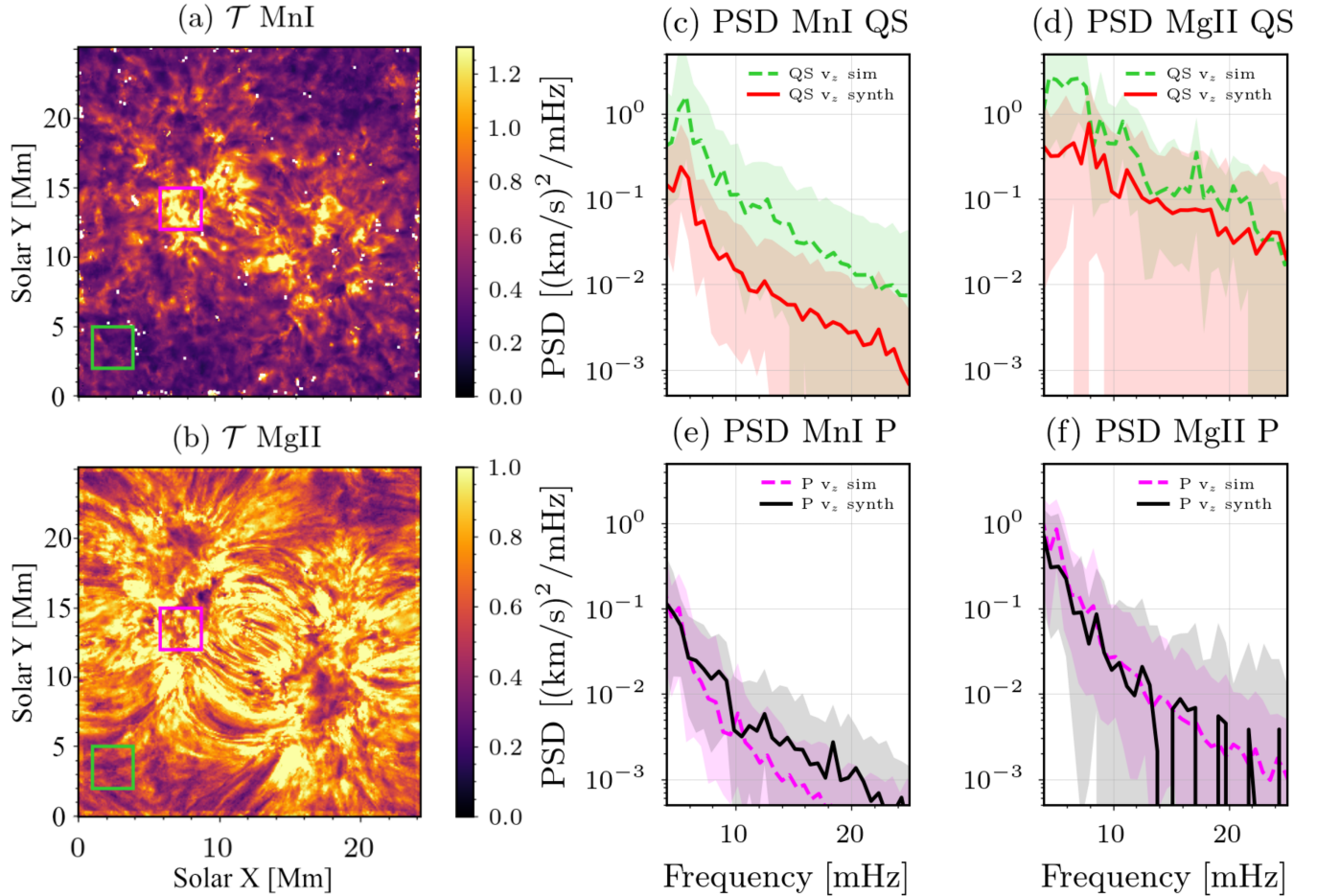


Figure 8. Attenuation coefficient \mathcal{T} maps in the Bifrost simulation for vertical velocity fluctuations between 5 and 20 mHz (panels (a)-(b)) based on the power spectral density of the observed and true plasma diagnostics (panels (c)-(f)). The top panel (a) shows the attenuation coefficient in the Mn I 280.1 nm line and the bottom panel (b) shows it for the Mg II k3 feature. The green and magenta regions correspond to the dark internetwork and enhanced network regions of interest. Panels (c)-(f) compare the power spectral density of the vertical velocity oscillatory power in the atmosphere at the formation height of the diagnostic (v_{sim}) and the Doppler velocity oscillatory power in the synthetic observations (v_{synth}) for the quiet Sun and plage regions. Note that the solid/dashed lines are the average of the distributions outlined as the colored squares in panels (a) and (b) and the shaded regions are the 10% / 90 % percentiles of the distributions.

ferent from previous work. This makes it more resistant to noise at the high-frequency limit, which can contribute to the observed Doppler velocities solely due to measurement errors. The attenuation coefficient maps for both Mn I 280.1 nm (panel (a)) and Mg II k3 (panel (b)) are presented in Figure 8. The attenuation coefficient varies significantly over the simulation domain and is partially correlated with the type of underlying solar features.

For the Mn I 280.1 nm line the attenuation coefficient is on the order of ~ 0.4 in the internetwork, which might be expected due to the strong variation in the heights being sampled of the Doppler velocity, as discussed in Section 5.1. In the case of the network regions, the at-

tenuation coefficient is closer to unity due to the fact that in these regions the height of formation changes significantly less, as shown in Figure 4 panel (c).

For the Mg II k3, the attenuation coefficient is in general higher compared with the Mn I lines. In the quieter regions the attenuation coefficient is lower (about ~ 0.6) and closer to unity in the network regions. In the case of the Mg II k3 (panel (b) of Figure 8), we see that the extended fibrillar structures in the simulation are clearly correlated with a higher transmission coefficient.

Panels (c)-(f) of Figure 8 present the power spectral density distributions of the synthetic observables and the actual plasma vertical velocity. In each panel, we plot the PSD of the vertical plasma velocity at the for-

mation height of the spectral line (v_{sim}) as well as the PSD of the Doppler velocity measured in the synthetic observables for solar region of interest. The lines are the mean of the PSD distributions and the shaded areas represent the 10th to 90th percentiles region of the distributions. For the Mn I line on average the power spectra of the observed Doppler velocity signals is attenuated with a constant shift, as seen previously in Paper I and discussed in previous work (Mein & Mein 1976; Bello González et al. 2009). However, for the plage-like regions the power spectra of the true plasma velocity and the one of the observed (synthetic) Doppler velocity are very similar and in some places the true velocity power exceeds the observed one. This is due to the fact that the passing wave fronts in the atmosphere introduce a jump-like change of the height of formation of the diagnostics, introducing jump-like signals in the measured Doppler velocity. This effect cannot be described with 1D semiempirical atmospheric modeling and we believe that it is important to be included in the accurate estimates of the wave fluxes, as it will increase the attenuation coefficient significantly for brighter regions, leading to lower acoustic flux estimates.

As is evident, the attenuation coefficient varies significantly and may depend in part on the solar feature being observed. This effect cannot be captured by static 1D models and will be definitely misrepresented by 1D hydrodynamic time-dependent models, as the obvious dependence on the simulated magnetic topology of the solar region helps determine its value. Hence, we believe that future estimations of the acoustic flux in the chromosphere should take the complicated nature of the transmission coefficient into consideration.

6. INFERRING THE ACOUSTIC WAVE FLUX

Spectral line	Density ρ [kg m^{-3}]	\mathcal{T}
QS Na I D ₁ 589.6 nm	$6.55 \cdot 10^{-7}$	0.68
QS Mn I 280.1 nm	$2.96 \cdot 10^{-8}$	0.37
QS Ca II 854.2 nm	$3.15 \cdot 10^{-9}$	0.56
QS Mg II k3	$8.55 \cdot 10^{-12}$	0.50
Plage Na I D ₁ 589.6 nm	$2.04 \cdot 10^{-6}$	0.91
Plage Mn I 280.1 nm	$5.82 \cdot 10^{-7}$	1.03
Plage Ca II 854.2 nm	$1.02 \cdot 10^{-8}$	0.89
Plage Mg II k3	$5.53 \cdot 10^{-11}$	0.80

Table 3. Density and attenuation coefficient values used for the acoustic flux estimation derived from the averages of the corresponding representative regions in Figure 4.

Based on the observational data presented in Section 2 and the numerical analysis in Sections 4 and 5,

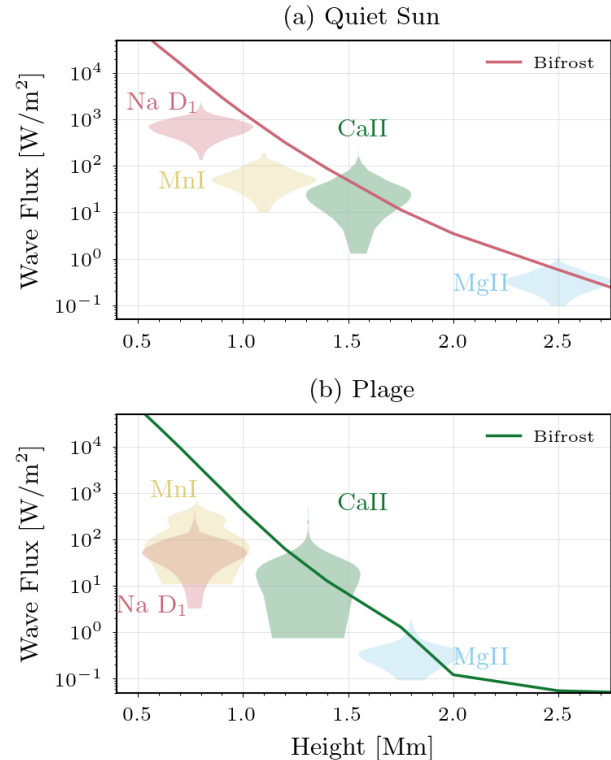


Figure 9. Acoustic flux in the different solar regions inferred from the IRIS observations presented in Figure 3. Panel (a) (top) presents the fluxes inferred for the internetwork region and the bottom panel (b) presents the fluxes inferred for the plage region. The straight lines show the acoustic fluxes in the Bifrost simulation at the respective height for the solar feature.

we have the required physical quantities to demonstrate the method for estimating the acoustic flux from the IRIS and IBIS observations, based on the synthetic observables derived from the Bifrost models. In Section 5 we showed that the internetwork and the plage regions exhibit different line formation characteristics, such as densities, velocity formation regions and attenuation of the wave signals, within the Bifrost simulation. In particular, the internetwork exhibits formation of the line that is significantly lower in density and has a lower transmission coefficient, compared to the active network elements.

Despite the variances in density shown in Figure 7 we chose to use the densities from Bifrost to compute acoustic wave fluxes. The mean formation properties employed for the different spectral lines are listed in Table 3 and were derived from averaging over the representative regions (shown as small boxes) in Figures 4 and 8. The attenuation coefficient values we obtained are significantly closer to unity than what previous authors have cited (Bello González et al. 2009; Abbasvand

et al. 2020a), which could be due to the different (and more realistic) modeling approach we employed. However, this will also lead to significantly lower estimates of the energy fluxes.

We used the average formation properties, as derived for regions of the simulation for the observed internetwork and plage regions described in Section 5. To calculate the wave fluxes, we adopt values of the density and the attenuation coefficient for the spectral lines separately for the two regions (shown as squares in Figure 4). The values are listed in Table 3.

Figure 9 presents the estimated wave fluxes, based on the calculated properties of the Bifrost simulations for the corresponding solar features. The top panel (a) shows the diagnostics for the internetwork and the bottom panel (b) shows the results for the plage regions. Overplotted are the Bifrost averaged acoustic flux as a function of height for the two regions for comparison.

For the case of the internetwork, the observation-derived values were generally lower than the acoustic fluxes retrieved directly from the simulations. This can be traced back to the difference in the observed and simulated Doppler velocity distributions in Figure 3. This might be due to a variety of reasons, including the magnetic field topology, incorrect driving of the p-modes in the bottom boundary of the simulations (Fleck et al. 2021) or incomplete physical treatment of the wave propagation and dissipation.

For the case of the plage observations, we saw that the lower chromosphere diagnostics were orders of magnitudes below the fluxes present in the simulation. Our modeling approach shows that the two independently observed lines of Na I D₁ and the Mn I 280.1 nm exhibit almost the same amount of acoustic flux at the about same formation height, acting as a self-consistency check. The wave fluxes derived from the middle and upper chromospheric diagnostics exhibit values closer to the ones derived from the Bifrost models.

In conclusion, our analysis shows that the observed Doppler velocities are lower than what were derived from synthetic line profiles calculated from simulations in the four spectral lines with formation heights spanning the chromosphere. Hence, the acoustic fluxes calculated from the observations, based on the simulation results, are also lower and likely insufficient to maintain the solar chromosphere in its quiescent state. This conclusion holds for both the quiet and plage chromospheres, compared to their respective radiative losses (Athay 1976). However, our analysis shows that any such conclusions are highly model dependent. In particular, the biggest systematic biases are the estimates of

the (average-value) densities and the attenuation coefficients.

7. DISCUSSION AND CONCLUSIONS

We present UV observations of waves in the solar chromosphere with the IRIS spacecraft. In particular, we examined the spectral lines of Mn I 280.1 nm (upper photosphere/lower chromosphere) and the Mg II k3 feature (upper chromosphere). Reduction steps, described in Section 2 enhance the data and the wave signatures were readily observed. The power spectra of the observed Doppler velocities and line-core intensity oscillations described in Section 3 exhibit the previously seen ubiquitous power law distributions. Comparing them with optical diagnostics from previous studies in the literature, we find agreement between the oscillatory properties of UV and optical diagnostics separately observed with IRIS and IBIS.

To interpret these observations, we relied on the 3D rMHD simulation Bifrost, that provided us with a detailed model of the lower solar atmosphere. This model includes detailed physics (non-LTE radiative losses and dynamic hydrogen ionization) important for wave propagation. We used the synthetic observables from Pereira et al. (2013) complemented with our own RH15D synthesis to understand the formation of the spectral diagnostics in question, described in Section 4. We found that the average density and heights of formation of the spectral lines differ significantly between the internetwork and network regions. Therefore, the height corresponding to the plasma velocity sampled by the Doppler measurement in these lines also changes with the underlying solar feature.

We compared the formation properties of the discussed spectral lines with other wave-modeling approaches used in the literature – the RADYN code and 1D semiempirical atmospheric perturbative approaches. In Section 5, we examined the differing formation properties resulting from the different modeling approaches and how they affect the inferred fluxes. In particular, we discuss how the measured Doppler velocities correspond to actual atmospheric velocities at different height for the different solar features in Section 5.1. In Bifrost we saw a strong a notable separation in the density of formation for the internetwork and the plage regions. The density of formation is significantly lower than the values found in previous work based on 1D semiempirical models. The value of the transmission coefficient is also significantly lower for the internetwork than for the enhanced network regions, too. However, it is significantly higher than values used in previous work, leading to a lower acoustic wave flux estimates.

Finally, in Section 6 we presented the inferred wave fluxes based on the physical parameters derived from the Bifrost simulations shown in Table 3. We used the values for internetwork and enhanced network separately. In our analysis the wave fluxes inferred from the observations are lower than the ones found in the simulation. In particular, the acoustic fluxes in the lower solar atmosphere, around the formation height of Mn I and Na D₁ lines are about a few hundred W/m². At the formation heights of the Mg II k3 feature, they are on the order of a few W/m². These results do not disagree per se with previous ones in the literature, more than what would be expected due to the systematic modeling biases described in Section 5.

Our work provides us with an example how more realistic simulations of the solar atmosphere are important for understanding the solar and stellar chromospheres. In particular, we show that the observed velocity field is not directly related to a singular height in the solar atmosphere. As shown in Figure 6, there is no good correlation between observed velocity amplitudes and the actual wave flux at the height of formation of the line. Because the velocity fluctuations are our key observable for atmospheric energetics, this means that our abilities to derive the amount of acoustic flux is severely limited. We show that the density of formation and transmission coefficients have to be adopted for different solar regions to be able to infer the acoustic flux.

However, given the complex structuring of the chromosphere, we will remain dependent on 3D rMHD models and the derived synthetic observables to provide the basis for determining certain statistical characteristics of different regions of the complex atmosphere. Yet, this makes our derivation of values like the acoustic flux dependent on the veracity and accuracy of those models, which in itself is a challenge to accurately ascertain. It

is necessary to be aware of the uncertainties and systematic biases carried forward by values based on these models.

Facilities: IRIS, DST(IBIS).

Software: SolarSoft; Matplotlib (Hunter 2007); NumPy (Oliphant 2006); SciPy (Virtanen et al. 2019); h5Py; RH15D (Pereira & Uitenbroek 2015). The Python and IDL scripts utilized for this project are available on the public repository of the author: https://github.com/momomolnar/IRIS_wave_signatures.

IRIS is a NASA small explorer mission developed and operated by LMSAL with mission operations executed at NASA Ames Research center and major contributions to downlink communications funded by ESA and the Norwegian Space Centre. Data in this publication were obtained with the facilities of the National Solar Observatory, which is operated by the Association of Universities for Research in Astronomy, Inc. (AURA), under cooperative agreement with the National Science Foundation. The authors would like to thank the anonymous referee, Amanda Alexander, Karen Slater, and Rahul Yadav whose input greatly improved the manuscript. MEM was supported for part of this work by the DKIST Ambassador Program, funding for which is provided by the National Solar Observatory, a facility of the National Science Foundation, operated under Cooperative Support Agreement number AST-1400405; and in part by a FINESST fellowship with grant number 80NSSC20K1505. This work utilized resources from the University of Colorado Boulder Research Computing Group, which is supported by the National Science Foundation (awards ACI-1532235 and ACI-1532236), the University of Colorado Boulder, and Colorado State University.

REFERENCES

- Abbasvand, V., Sobotka, M., Heinzl, P., et al. 2020a, *ApJ*, 890, 22
- Abbasvand, V., Sobotka, M., Švanda, M., et al. 2021, *A&A*, 648, A28
- . 2020b, *A&A*, 642, A52
- Allred, J. C., Hawley, S. L., Abbett, W. P., & Carlsson, M. 2005, *ApJ*, 630, 573
- Allred, J. C., Kowalski, A. F., & Carlsson, M. 2015, *ApJ*, 809, 104
- Anan, T., Schad, T. A., Kitai, R., et al. 2021, *ApJ*, 921, 39
- Aschwanden, M. J. 2019, *New Millennium Solar Physics*, Vol. 458 (Springer Nature Switzerland AG), doi:10.1007/978-3-030-13956-8
- Athay, R. G. 1976, *The solar chromosphere and corona: Quiet sun*, Vol. 53 (Dordrecht: Reidel), doi:10.1007/978-94-010-1715-2
- Bello González, N., Flores Soriano, M., Kneer, F., & Okunev, O. 2009, *A&A*, 508, 941
- Bergemann, M., Gallagher, A. J., Eitner, P., et al. 2019, *A&A*, 631, A80

- Bertschinger, E., & Chevalier, R. A. 1985, *The Astrophysical Journal*, 299, 167
- Biermann, L. 1946, *Naturwissenschaften*, 33, 118
- Bjørgen, J. P., Leenaarts, J., Rempel, M., et al. 2019, *A&A*, 631, A33
- Bray, R. J., & Loughhead, R. E. 1974, *The solar chromosphere* (London: Chapman and Hall)
- Carlsson, M., De Pontieu, B., & Hansteen, V. H. 2019, *ARA&A*, 57, 189
- Carlsson, M., Hansteen, V. H., Gudiksen, B. V., Leenaarts, J., & De Pontieu, B. 2016, *A&A*, 585, A4
- Carlsson, M., & Stein, R. F. 1992, *ApJL*, 397, L59
- Carlsson, M., Hansteen, V. H., de Pontieu, B., et al. 2007, *PASJ*, 59, S663
- Cavallini, F. 2006, *SoPh*, 236, 415
- da Silva Santos, J. M., Danilovic, S., Leenaarts, J., et al. 2022, *A&A*, 661, A59
- de Pontieu, B. 2004, in *ESA Special Publication*, Vol. 547, *SOHO 13 Waves, Oscillations and Small-Scale Transients Events in the Solar Atmosphere: Joint View from SOHO and TRACE*, ed. H. Lacoste, 25
- De Pontieu, B., Title, A. M., Lemen, J. R., et al. 2014, *SoPh*, 289, 2733
- Díaz Baso, C. J., de la Cruz Rodríguez, J., & Leenaarts, J. 2021, *A&A*, 647, A188
- Felipe, T., Kuckein, C., & Thaler, I. 2018, *A&A*, 617, A39
- Felipe, T., & Socas-Navarro, H., 2023, *ArXiv*, 2301.03273
- Fleck, B., Carlsson, M., Khomenko, E., et al. 2021, *Philosophical Transactions of the Royal Society of London Series A*, 379, 20200170
- Fontenla, J. M., Harder, J., Livingston, W., Snow, M., & Woods, T. 2011, *Journal of Geophysical Research (Atmospheres)*, 116, D20108
- Fossum, A., & Carlsson, M. 2005, *Nature*, 435, 919
- . 2006, *ApJ*, 646, 579
- Gudiksen, B. V., Carlsson, M., Hansteen, V. H., et al. 2011, *A&A*, 531, A154
- Hegglund, L. and Hansteen, V. H. and De Pontieu, B. and Carlsson, M., 2011, *ApJ*, 743, 2
- Hofmann, R. A., Reardon, K. P., Milic, I., et al. 2022, *ApJ*, 933, 244
- Hunter, J. D. 2007, *Computing In Science & Engineering*, 9, 90
- Innes, D. E., Inhester, B., Axford, W. I., & Wilhelm, K. 1997, *Nature*, 386, 811
- Jefferies, S. M., Fleck, B., Murphy, N., & Berrilli, F. 2019, *The Astrophysical Journal Letters*, 884, L8
- Kayshap, P., Murawski, K., Srivastava, A. K., Musielak, Z. E., & Dwivedi, B. N. 2018, *MNRAS*, 479, 5512
- Kurucz, R. L. 2018, in *Astronomical Society of the Pacific Conference Series*, Vol. 515, *Workshop on Astrophysical Opacities*, 47
- Leenaarts, J., Pereira, T., & Uitenbroek, H. 2012, *A&A*, 543, A109
- Leenaarts, J., Pereira, T. M. D., Carlsson, M., Uitenbroek, H., & De Pontieu, B. 2013, *ApJ*, 772, 90
- Leenaarts, J., Rutten, R. J., Reardon, K., Carlsson, M., & Hansteen, V. 2010, *ApJ*, 709, 1362
- Linsky, J. L. 2017, *ARA&A*, 55, 159
- Louis, R. E., Prasad, A., Beck, C., Choudhary, D. P., & Yalim, M. S. 2021, *A&A*, 652, L4
- Mein, N., & Mein, P. 1976, *SoPh*, 49, 231
- Molnar, M. E., Reardon, K. P., Chai, Y., et al. 2019, *ApJ*, 881, 99
- Molnar, M. E., Reardon, K. P., Cranmer, S. R., et al. 2021, *ApJ*, 920, 125
- Morosin, R., de la Cruz Rodríguez, J., Díaz Baso, C. J., & Leenaarts, J. 2022, *arXiv e-prints*, arXiv:2203.01688
- Oliphant, T. 2006, *NumPy: A guide to NumPy, USA*: Trelgol Publishing. <http://www.numpy.org>
- Pereira, T. M. D., Leenaarts, J., De Pontieu, B., Carlsson, M., & Uitenbroek, H. 2013, *ApJ*, 778, 143
- Pereira, T. M. D., & Uitenbroek, H. 2015, *A&A*, 574, A3
- Pietrow, A. G. M., Kiselman, D., de la Cruz Rodríguez, J., et al. 2020, *A&A*, 644, A43
- Reardon, K. P., & Cavallini, F. 2008, *A&A*, 481, 897
- Reardon, K. P., Lepreti, F., Carbone, V., & Vecchio, A. 2008, *ApJL*, 683, L207
- Rimmele, T. R., Warner, M., Keil, S. L., et al. 2020, *SoPh*, 295, 172
- Roupe van der Voort, L., De Pontieu, B., Scharmer, G. B., de la Cruz Rodríguez, J., et al. 2017, *ApJ*, 851, 6
- Sadeghi, R., & Tavabi, E. 2022, *MNRAS*, 512, 4164
- Schatzman, E. 1949, *Annales d'Astrophysique*, 12, 203
- Schou, J., Scherrer, P. H., Bush, R. I., et al. 2012, *SoPh*, 275, 229
- Sobotka, M., Heinzel, P., Švanda, M., et al. 2016, *ApJ*, 826, 49
- Socas-Navarro, H. 2005, *ApJL*, 633, L57
- Tousey, R. 1967, *ApJ*, 149, 239
- Uitenbroek, H. 2001, *ApJ*, 557, 389
- Ulmschneider, P., Rammacher, W., Musielak, Z. E., & Kalkofen, W. 2005, *ApJL*, 631, L155
- Vecchio, A., Cauzzi, G., Reardon, K. P., Janssen, K., & Rimmele, T. 2007, *A&A*, 461, L1
- Virtanen, P., Gommers, R., Oliphant, T. E., et al. 2019, *arXiv e-prints*, arXiv:1907.10121

- Wedemeyer-Böhm, S., Steiner, O., Bruls, J., & Rammacher, W. 2007, in *Astronomical Society of the Pacific Conference Series*, Vol. 368, *The Physics of Chromospheric Plasmas*, ed. P. Heinzel, I. Dorotovič, & R. J. Rutten, 93
- Withbroe, G. L., & Noyes, R. W. 1977, *ARA&A*, 15, 363
- Wunnenberg, M., Kneer, F., & Hirzberger, J. 2002, *A&A*, 395, L51
- Zaqarashvili, T. V., & Skhirtladze, N. 2008, *ApJL*, 683, L91